Journal of Rare Earths 40 (2022) 226–233

Contents lists available at ScienceDirect

Journal of Rare Earths

journal homepage: http://www.journals.elsevier.com/journal-of-rare-earths

Red-emitting $CaWO_4:Eu^{3+},Tm^{3+}$ phosphor for solid-state lighting: Luminescent properties and morphology evolution☆

L.X. Lovisa [a,*], J.M.P. da Silva [b], A.A.G. Santiago [b], M. Siu Li [c], E. Longo [d], C.A. Paskocimas [b], M.R.D. Bomio [b], F.V. Motta [b]

[a] Institute of Physics and Chemistry, Federal University of Itajubá (UNIFEI), Itajubá, MG, 37500-903, Brazil
[b] LSQM – Laboratory of Chemical Synthesis of Materials – Department of Materials Engineering, Federal University of Rio Grande Do Norte, P.O. Box 1524, 59078-900, Natal, RN, Brazil
[c] IFSC, USP, Av. Trabalhador São Carlense, 400, CEP 13566-590, São Carlos, SP, Brazil
[d] CDMF-LIEC, UFSCar, P.O. Box 676, 13565-905, São Carlos, SP, Brazil

ARTICLE INFO

Article history:
Received 7 August 2020
Received in revised form
18 December 2020
Accepted 12 January 2021
Available online 20 January 2021

Keywords:
$CaWO_4:Eu^{3+},Tm^{3+}$
microwave-assisted hydrothermal method
Photoluminescence
Red phosphor
Rare earths

ABSTRACT

$CaWO_4:xEu^{3+},yTm^{3+}$ crystals were obtained by facile synthesis at low temperature by the microwave-assisted hydrothermal method (MAH). The phase formation, morphology, luminescent properties and energy transfer were investigated. The X-ray diffraction (XRD) results show the formation of a scheelite-like tetragonal structure without the presence of secondary phases. The growth mechanism of hierarchical microstructures based on self-assembly and Ostwald-ripening processes was evaluated, obtaining different types of morphologies. The luminescence spectra of $CaWO_4:Eu^{3+},Tm^{3+}$ at 325 nm excitation show the predominance of red emission at the $^5D_0 \rightarrow {}^7F_2$ (Eu^{3+}) transition at 624 nm. This feature signals dominant behavior of the electric dipole type. The presence of Tm^{3+} is notably evident in the absorption spectra by the related excitation transitions: $^3H_6 \rightarrow {}^1G_4$, $^3H_6 \rightarrow {}^3F_3$ and $^3H_6 \rightarrow {}^3H_4$. Color parameters are discussed to characterize $CaWO_4:Eu^{3+},Tm^{3+}$ emission. The study of the emission spectrum as a function of the concentration of Eu^{3+} (x mol%) and Tm^{3+} (y mol%) indicates that the $CaWO_4:Eu^{3+},Tm^{3+}$ phosphors show stronger red emission intensity and exhibit the CIE value of $x = 0.63$ and $y = 0.35$. The photoluminescence results show 97% high color purity for $CaWO_4$:4 mol%Eu^{3+}, a high CRI (92%) and a low CCT of 1085 K. These results demonstrate that the $CaWO_4:Eu^{3+},Tm^{3+}$ red phosphors are promising as color converters for application in white light-emitting diodes and display devices.

1. Introduction

The advancement in the production of efficient white light in the use of lighting, which meets the desirable photometric parameters, is a constant search for the solid state lighting industry. One of the first commercial WLEDs to be synthesized was composed of a blue LED chip with yellow phosphor $Y_3Al_5O_{12}:Ce^{3+}$.[1,2] The operational limitation of this material was its low color rendering index (CRI) due to the absence of red phosphorus. To reverse this difficulty, the most promising method to achieve high-quality WLEDs is the combination of red, blue and green phosphors with near-ultraviolet (NUV) LED chips or blue LED chips.[3,4] However, this new phosphor profile requires a red component of high color purity.[5]

The development of red phosphor is of fundamental importance for application in the constitution of WLEDs ensuring its quality. For this reason, several matrices have been produced to meet this demand. Guo et al.[6] observed an energy transfer from Sm^{3+} to Eu^{3+} of $Ba_3Bi(PO_4)_3$ with good thermal stability and a high color purity of 88.9%. Huan et al.[7] improved the photoluminescent properties of $KBaLu(MoO_4)_3$ by increasing the concentration of Eu^{3+}. Zheng et al.[8] produced $NaBaBO_3:Sm^{3+}$ by the solid state reaction and compared to commercial yellow phosphor $YAG:Ce^{3+}$ obtained a higher level of color purity.

Included in this context, the family of metal tungstates (AWO_4, A = Pb, Zn, Ca, Ba, Sr) has shown satisfactory results as potential candidates for these technological applications due to their optical properties. Tungstates have broad and intense absorption bands ensuring the charge transfer of oxygen (O^{2-}) to metal (W^{6+}) in the

☆ **Foundation item:** Project supported by National Council for Scientific and Technological Development – CNPq (303,604 / 2018–2) and the Coordination for the Improvement of Higher Education Personnel (CAPES) - Brazil.
* Corresponding author.
E-mail address: lauraengmat@hotmail.com (L.X. Lovisa).

https://doi.org/10.1016/j.jre.2021.01.005
1002-0721/

UV and visible region.[9] The NUV chip with excitable phosphors therefore is another attractive combination for white light generation. Rare earths doped tungstates phosphor is a good candidate for NUV white LED owing to its good photoluminescence properties and chemical-physical stabilities.

In particular, $CaWO_4$ demonstrates excellent performance as a rare earth ion host matrix for photoluminescence studies because of its physico-chemical properties.[10] $CaWO_4$ can be doped and activated with NUV-blue light-absorbing ions for applications in WLEDs due to the efficient energy transfer of RE^{3+} (rare earth) from tetragonal tungstate groups [WO_4] to the activator ions.[11] The increased efficiency and observed changes in the spectral emission range of PL can be verified from the control of $CaWO_4$ particle size and shape. In addition to morphological aspects, the presence of dopants in the host matrix crystal lattice can significantly influence the electronic band structures.[12]

The control of particle morphologies is a factor that greatly influences the photoluminescent behavior of the material. The growth of the crystal can be carried out with the objective of obtaining a final desirable morphology based on protocols adopted in the experimental conditions (precursor reagents, surfactants, pH, synthesis time and temperature). This control in morphology may be associated with some properties of interest that are more evident in a given direction or face of the crystal.[13] According to Lee,[14] hierarchical structures consist of higher dimensional arrangements formed by smaller construction units with small size (that is, nanoparticles, nanoblasts). These new materials that have hierarchical structures present new characteristics as a result of the union of the crystal forming units.[15]

As a consequence of the low levels exhibited by commercial red phosphor compared to blue and green phosphors, and because the red emitting components have greater effects on the photoluminescent properties for WLEDs, the present work aimed to investigate the photoluminescent behavior of $CaWO_4$ associated with the effects of dopants Tm^{3+} and Eu^{3+} in terms of color quality parameters. The $CaWO_4$:Eu^{3+},Tm^{3+} crystal growth proposal is presented and discussed, showing the evolution of the morphologies based on the self-assembly and Ostwald-ripening (OR) processes.

2. Experimental

2.1. Materials

Sodium tungsten oxide dihydrate ($Na_2WO_4{\cdot}2H_2O$, 95%, Alfa Aesar), calcium nitrate ($Ca(NO_3)_2{\cdot}4H_2O$, 99%, Alfa Aesar), europium oxide (Eu_2O_3, 99%, Aldrich), thulium oxide (Tm_2O_3, 99%, Aldrich), nitric acid (HNO_3) (Synth), ammonium hydroxide (NH_4OH) (Synth) and distilled water were used as received for the preparation of the $CaWO_4$ and $CaWO_4$:Eu^{3+},Tm^{3+} particles.

2.2. Preparation of $CaWO_4$:Eu^{3+},Tm^{3+} particles

Initially, the Tm_2O_3 and Eu_2O_3 oxides were dissolved separately in 10 mL of nitric acid to obtain their respective nitrate. This element is insoluble in the reaction medium once in the oxide form. Two precursor solutions were prepared for the synthesis of the $CaWO_4$ and $CaWO_4$:$x$$Eu^{3+}$,$y$$Tm^{3+}$ (x:y = 4:0, 3:1, 2:2, 1:3 in molar ratio) particles: one of tungsten (solution A) and the other of calcium (solution B), with a molar ratio of 1:1. The starting reagent was dissolved in 40 mL of distilled water for both solutions. Solution B was added to the solution by dripping it and under constant magnetic stirring. Then the dopants were added one at a time. Finally, NH_4OH was added to the solution to stabilize its pH at 7 for observing the formation of the precipitate. The mixture was transferred into a Teflon autoclave which was sealed and placed into a microwave hydrothermal system (2.45 GHz, maximum power of 800 W). Microwave hydrothermal conditions were kept at 140 °C for 30 min using a heating rate fixed at 25 °C/min. The pressure in the autoclave was stabilized at 3.0×10^5 Pa. After the microwave-hydrothermal treatment, the autoclave was cooled to room temperature. The resulting solution was washed with deionized water several times and the white precipitates were finally collected. Using the same experimental conditions, the obtained powders were dried in a conventional furnace at 100 °C for 24 h.

2.3. Characterizations

The $CaWO_4$ and $CaWO_4$:Eu^{3+},Tm^{3+} particles were structurally characterized by X-ray diffraction (XRD) using a Shimadzu XRD 7000 instrument with Cu Kα radiation ($\lambda = 0.15406$ nm) in the 2θ range from 10° to 80° at a scanning rate of 0.02 s^{-1}. Raman spectroscopy measurements were recorded using a T-64000 spectrometer (Jobin-Yvon, France) triple monochromator coupled to a CCD detector. The spectra were performed using a 514.5 nm wavelength of an argon ion laser, keeping its maximum output power at 8 mW. The morphologies were investigated using field-emission gun scanning electron microscopy (FEG-SEM; Carl Zeiss, Supra 35-VP Model, Germany) operated at 6 kV. The UV–Vis diffuse reflectance spectrum was measured at room temperature using a UV–Vis spectrometer. The photoluminescence (PL) spectra were acquired with an Ash Monospec 27 monochromator (Thermal Jarrel, U.S.A.) and a R4446 photomultiplier (Hamamatsu Photonics, U.S.A.). The 325 nm beam of a krypton ion laser (Coherent Innova 90 K) was used as the excitation source while its maximum output power was kept at 200 mW. All measurements were performed at room temperature.

3. Results and discussion

3.1. XRD analyses

Fig. 1 shows the XRD patterns of $CaWO_4$ and $CaWO_4$:Eu^{3+},Tm^{3+} series synthesized by the microwave assisted hydrothermal (MAH) method. All diffraction peaks are well indexed to the $CaWO_4$ tetragonal structure based on the JCPDS card No. 85–0443 (space group: $I41/a$). It was found that there is no secondary phase peak in the samples. The concentration of dopants did not cause significant

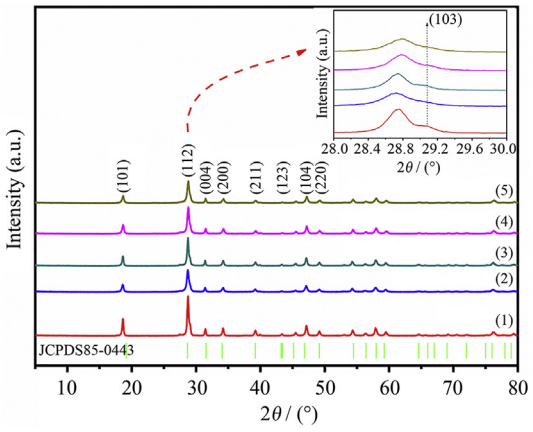

Fig. 1. XRD patterns of samples $CaWO_4$ (1), $CaWO_4$:4 mol%Eu^{3+} (2), $CaWO_4$:3 mol% Eu^{3+},1 mol%Tm^{3+} (3), $CaWO_4$:2 mol%Eu^{3+},2 mol%Tm^{3+} (4), $CaWO_4$:1 mol%Eu^{3+},3 mol% Tm^{3+} (5) and displacement and enlargement of the plane (112) by the effect of doping.

changes in the $CaWO_4$ matrix, because the ionic rays of Eu^{3+} (0.108 nm) and Tm^{3+} (0.105 nm) presented very close values to the ionic radius of Ca^{2+} (0.112 nm). The introduction of dopants widens the full width at half maximum (FWHM) of the plane (112) by 28.74°, which increases from 0.166° ($CaWO_4$) to 0.280° ($CaWO_4$:4 mol%Eu^{3+}) as shown in the detail of Fig. 1. Eu^{3+} (Tm^{3+}) is introduced at the Ca site of the $CaWO_4$ matrix as indicated in the Kröger–Vink reactions (1) and (2):

$$CaWO_4 + Eu^{3+} \rightarrow Eu_{Ca}^{+} + V_{Ca}^{2+} + 4O_O^X + Ca_{Ca}^X \quad (1)$$

$$CaWO_4 + Tm^{3+} \rightarrow Tm_{Ca}^{+} + V_{Ca}^{2+} + 4O_O^X + Ca_{Ca}^X \quad (2)$$

Due to the $Ca^{2+} \rightarrow Eu^{3+}$ (Tm^{3+}) substitution, the emergence of calcium vacancies (V_{Ca}^{2+}) occurs as a mechanism to neutralize the compound charge.

3.2. Rietveld refinement analyses

The $CaWO_4$ (and $CaWO_4$:Eu^{3+},Tm^{3+}) structure parameters, unit cell volume, bond length and bond angles were obtained and calculated by the Rietveld refinement method using the GSAS (General Structure Analysis System) program[16] with graphical interface EXPGUI. Rietveld refinement graphs in Fig. S1 and all data on structural refinement in Table S1 are presented in the supplementary material.

The values of the lattice parameters and the unit cell volume are consistent with the values found in the literature.[17] The slight variations in values are associated with the substitution of Ca^{2+} by Eu^{3+}/Tm^{3+} ions due to the difference in their electronic densities (r (Ca^{2+}) = 0.112 nm vs. r (Eu^{3+}) = 0.108 nm and r (Tm^{3+}) = 0.105 nm). Synthesis conditions such as temperature, processing time, heating rate, solvents, pH, chemical precursors interfere with the organization of clusters [CaO_8], [EuO_8], [TmO_8] and [WO_4] within the scheelite structure. These distortions may result in the emergence of structural defects (oxygen vacancies, bond distortion, stresses and deformation in the crystal lattice) in materials.[18] Atomic positions from the Rietveld refinement are listed in Table S2 in the supplementary material.

3.3. FT-Raman spectra analyses

Fig. 2 shows the Raman spectra for $CaWO_4$ and $CaWO_4$:Eu^{3+},Tm^{3+} series synthesized by the MAH method.

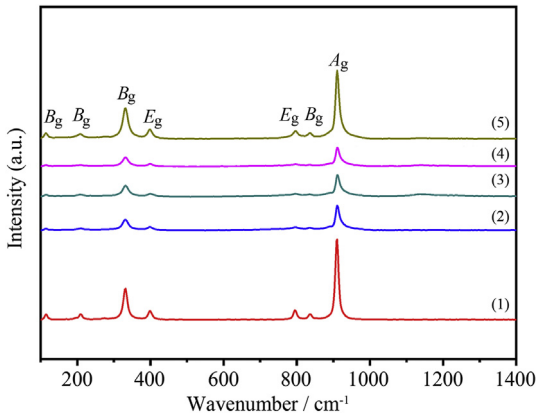

Fig. 2. Raman spectra of $CaWO_4$ (1), $CaWO_4$:4 mol%Eu^{3+} (2), $CaWO_4$:3 mol%Eu^{3+},1 mol%Tm^{3+} (3), $CaWO_4$:2 mol%Eu^{3+},2 mol%Tm^{3+} (4) and $CaWO_4$:1 mol%Eu^{3+},3 mol%Tm^{3+} (5).

According to the study of group theory, there are four vibration modes for ideal symmetry T_d regarding the scheelite structure as represented by Eq. (3):

$$\Gamma = A_1(\nu_1) + E(\nu_2) + F_2(\nu_3) + F_2(\nu_4) \quad (3)$$

Each mode is associated with a specific type of vibration that occurs at the bonds between atoms. Vibration $A_1(\nu_1)$ is the symmetrical elongation mode, $F_2(\nu_3)$ is the antisymmetrical elongation mode and vibrations $E(\nu_2)$ and $F_2(\nu_4)$ are flexion modes. Because the smaller symmetry of the $CaWO_4$ factor groups and the tetrahedral point groups are not ideal, the $E(\nu_2)$ mode is doubly degenerate and the $F_2(\nu_4)$ vibrations are triple degenerate, producing 26 vibrations[19] as represented by Eq. (4):

$$\Gamma = 3A_g + 5A_u + 5B_g + 3B_u + 5B_g + 5E_u \quad (4)$$

According to the results presented in Fig. 2, it is possible to identify bands referring to [WO_4] Raman active internal modes, as represented by: ν_4 (B_g), ν_4 (E_g), ν_3 (E_g), ν_3 (B_g), ν_1 (A_g) and the bands associated with external modes are characterized by: $T - (2B_g)$.[20] Table S3 in the supplementary material records the normal modes of Raman vibration found in this work compared to the results obtained in other studies in the literature.

The active Raman modes are very characteristic and well defined, so that the $CaWO_4$ and $CaWO_4$:Eu^{3+},Tm^{3+} particles obtained by the MAH method are well ordered structurally. According to Gracia et al.,[12] the indicator of distortion around [WO_4] is caused by the vibration A_g resulting from the Davydov splitting of the (A_1) ν_1 free tetrahedral anion.

3.4. FEG-SEM images analyses

Fig. 3 shows the FEG-SEM images of the $CaWO_4$ and $CaWO_4$:Eu^{3+},Tm^{3+} series particles obtained by the MAH method. Based on FEG-SEM images it is possible to understand the evolution and growth mechanism of these crystals.

Fig. 3 shows the different morphologies for $CaWO_4$ and $CaWO_4$:Eu^{3+},Tm^{3+} crystals. Fig. 3(a) represents the morphology of $CaWO_4$, in which the predominance of microspheres formed by small particles is verified. The microspheres vary in diameter size from 3.20 to 5 μm. Fig. 3(b–f) refer to the $CaWO_4$:Eu^{3+},Tm^{3+} series. Fig. 3(b) shows dumbbell-like particle with a 4.15 μm length and a 1.50 μm diameter. The high resolution image shows that the crystals are made up of a smaller particle set. These particles are highly oriented and associated with each other allowing for a recognizable final shape. The self-assembly process of the smaller particles enables anisotropic growth of $CaWO_4$:Eu^{3+},Tm^{3+} crystals.[21] At a later stage, crystal growth can be governed by the Ostwald-Ripening (OR) process.[22] The precipitated crystals undergo an evolution through the OR process, which corresponds to the mass transfer of the smaller crystals to the larger crystals, causing an increase in the average crystal size. The main driving force for the OR process is the minimization of surface energy.[23] This effect is perfectly correlated with the more stable morphological characteristics of the crystals, observing the temperature, pressure and pH conditions that were submitted. Fig. 3(c) presents a double broccoli-like form, identifying the growth process of the particles. The ends of the dumbbells grow expressively, signaling that the growth occurs faster in these places, causing both ends to lean towards each other. Fig. 3(d) shows microspherical type morphology. This morphology is the result of a self-assembly process formed by numerous submicrodumbbells.[24] The submicrodumbbells are partially assembled in clusters, the formed clusters participate in the growth of crystals by OR reaching spherical superstructures. The micro-axes continue to be mounted in spherical clusters and the typical 3D

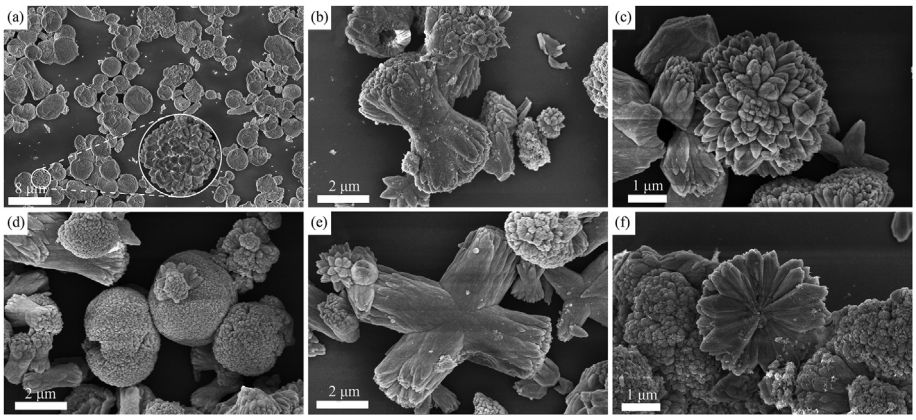

Fig. 3. FEG-SEM images of $CaWO_4$ (a), $CaWO_4$:4 mol%Eu^{3+} (b, c), $CaWO_4$:3 mol%Eu^{3+},1 mol%Tm^{3+} (d, e) and $CaWO_4$:2 mol% Eu^{3+},2 mol%Tm^{3+} (f).

microspherical structure is formed, as shown in Fig. 3(d). The formation of the $CaWO_4$:Eu^{3+},Tm^{3+} microspheres is obtained by a self-assembly process that generates an isotropic growth of the crystals.[25] Fig. 3(e) shows the union of two dumbbells connected by the central region, verifying a radial growth in the ends of the dumbbells. With growth, new self-assembly tips emerge from the structure and each petal is joined by a center, gaining a microflower morphology as shown in Fig. 3(f). The growth of these petals happens at a later stage due to the OR process. In short, it is reasonable to consider that the self assembly and OR processes contributed to forming the different types of $CaWO_4$:Eu^{3+},Tm^{3+} morphologies.

A schematic illustration for the $CaWO_4$:Eu^{3+},Tm^{3+} crystal growth proposal is shown in Fig. 4. A strong force of attraction occurs between ions due to the difference in electron density between Ca^{2+} (Tm^{3+}/Eu^{3+}) and $[WO_4]^{2-}$ ions, which results in the formation of primary nuclei.[26] The increased precipitation rate causes the aggregation process of numerous small nuclei. The self-assembly mechanism occurs from these cores due to the particular conditions employed in the synthesis of the material, such as: pH, temperature, pressure and aqueous solvent used. Particle growth then occurs from a preferential direction at a later stage represented by anisotropic behavior. In a subsequent moment, these oriented particles come together and appear to have a dumbbell

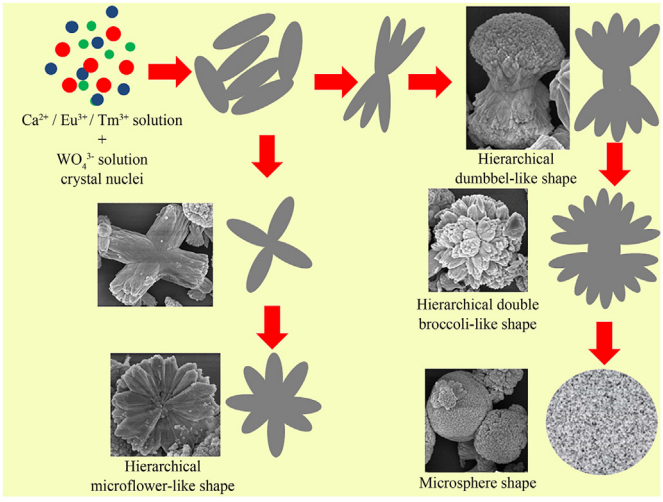

Fig. 4. Illustrative scheme of particle growth and formation of different hierarchical morphologies.

aspect with more pronounced growth of the ends of the particles. Growth is then governed by the OR process in the resulting stages, so it is possible to observe double broccoli-like, microsphere and microflower morphologies, as shown in the representative scheme of Fig. 4.

The OR process is governed by thermodynamic foundations which justify the deposition of smaller crystals into larger crystals because the smaller crystals have lower energy stability, favoring the growth of larger crystals.[27] Gonçalves et al.[28] stated that $CaWO_4$:Eu^{3+} crystals have a predominantly anisotropic growth behavior, but with increasing amount of Eu^{3+} they have a tendency for isotropic growth. According to the authors, unidirectional growth is attributed to different interaction rates between crystal surfaces, leading to a mechanism of continuous growth on a specific surface.[29]

Fig. S2 in the supplementary material shows the chemical composition of $CaWO_4$:2 mol%Eu^{3+},2 mol%Tm^{3+} performed by dispersive energy X-ray spectroscopy (EDS).

3.5. UV–Vis diffuse reflectance spectroscopy analyses

$CaWO_4$:Eu^{3+},Tm^{3+} UV–Vis reflectance spectra are shown in Fig. S3 in the supplementary material. According to the results, all samples had photoabsorption properties in the range of 200–450 nm. According to Abraham et al.[30] and based on the functional theory of density, the upper part of the valence band on the tungstate scheelite and wolframite structures mainly consists of the O^{2-} (2p) states and the conduction band is dominated by the W^{6+} (5 d) states.

Diffuse reflectance spectra transformed into absorption spectra by the Kubelka–Munk method (5) are shown in Fig. S4 in the supplementary material.

$$\alpha = \frac{(1-R)^2}{2R} \tag{5}$$

where α is the absorption coefficient and R is the reflectivity. From this relationship it is possible to estimate the gap band interval between the powdery diffuse reflection spectra.[31] It is then possible to determine the gap energy from the Tauc ratio according to Eq. (6):

$$\alpha \propto (h\nu - E_g)^n \tag{6}$$

where E_g is the gap energy, $h\nu$ photon energy and n an index that assumes different values according to the nature of the electronic

transition responsible for reflection (n = ½ for direct allowed transitions, $n = 2$ for indirect allowed transitions, $n = 3/2$ for direct prohibited transitions and $n = 3$ for indirect prohibited transitions). According to the theoretical calculations reported in the literature,[32] $CaWO_4$ microcrystals exhibit an optical absorption spectrum governed by direct electronic transitions. From the extrapolation of the line in the linear region in the curves of Fig. S4, the gap energy values for $CaWO_4$ and $CaWO_4$:Eu^{3+},Tm^{3+} were estimated, and the values found are between 3.20 and 4.14 eV. These values are below those found in other works.[12,18,22]

3.6. Photoluminescence properties

Fig. 5(a, b) represent the photoluminescence emission spectra of $CaWO_4$ and $CaWO_4$:Eu^{3+},Tm^{3+} obtained by the MAH method. The samples were excited by a 325 nm wavelength laser at room temperature. The $CaWO_4$ spectrum in Fig. 5(a) has a broad emission range of 368–738 nm centered at around 515 nm. This broadband spectrum characteristic is correlated to the transfer transitions between clusters $[WO_3]$ and $[WO_4]$,[28] which occur at energy levels close to the valence and conduction bands, this configuration occurs in the bluish green region. The multiphonic or multilevel process involves the participation of numerous energy states within the band interval.[33]

According to the theoretical study by Orhana et al.,[34] the load difference between the WO_4 and WO_3 is 0.43e. Due to this polarization, the appearance of holes and trapped electrons is promoted, causing photoluminescence at room temperature as metallic tungstates (AMO_4). The coexistence of localized levels and this charge gradient creates favorable conditions for the self-trapping of excitons before the emission of luminescence photons.[34] In such way the charge transfer between the WO_4 and WO_3 clusters is related to the existence of ordered and disordered clusters in the microstructure, responsible for the emission of photoluminescence. Patil et al.[35] reported the transitions present in $CaWO_4$ in their study of $BaWO_4/CaWO_4$ nanocomposite. The configuration of the electron in the $(WO_4)^{2-}$ ground state with T_d symmetry was performed using molecular orbital calculations.[36] Lower excited states are $^1T_2$, $^1T_1$, $^3T_2$, $^3T_1$. Radiative transitions occur from $^3T_2$ and $^3T_1$ states. The fundamental absorption edge of $CaWO_4$ is due to $^1A_1 \rightarrow {}^1T_2$, $^1T_1$ transitions. Maheshwary et al.[37] attributed the PL emission of $SrWO_4$:Eu^{3+} to the presence of defects in the band interval, which favor electronic transitions within localized energy levels. The red emission of $SrWO_4$:Eu^{3+} was correlated to distortions in short and long distances and in tetrahedrons $[WO_4]^{2-}$ due to the different angles between O–W–O.

In Fig. 5(b), $CaWO_4$:Eu^{3+},Tm^{3+} shows a group of Eu^{3+} emission lines showing f–f type electronic transitions: $^5D_0 \rightarrow {}^7F_J$ ($J = 0, 1, 2, 3$ and 4) located respectively at 544, 601, 624, 660 and 708 nm.[38] Tm^{3+} transitions are not visible in the PL emission spectra, however the presence of Tm^{3+} in $CaWO_4$ is confirmed by the results presented in the chemical analysis by dispersive energy X-ray spectroscopy (Fig. S2) and in the reflectance spectra UV–Vis (Fig. S3) which exhibit Tm^{3+}transitions. The excitation wavelength is also important for what the transitions of the lanthanide ions appeared clearly. According to the studies,[39] they observed that the Tm^{3+} transitions are favored when excited at a longer wavelength.

From the PL spectra in Fig. 5(b), it is observed that the energy transfer between $[WO_4]^{2-}$ to the activating ion Eu^{3+} occurs successfully. It is observed that matrix interference only occurs in the $CaWO_4$:4 mol%Eu^{3+} sample due to the presence of a wide band between 475 and 725 nm which are in turn due to the structural defects and distortion of $CaWO_4$. Many Eu^{3+} doped scheelite-related phosphors have also been extensively studied and revealed a non-radiative mechanism for the energy transfer to the activating ion.[40] The introduction of Eu^{3+} ions into the $CaWO_4$ structure significantly alters the behavior of luminescence spectra due to the formation of emission centers which generate a specific red light when excited under UV light.[41] Tungstates doped with rare earth ions have special properties due to $[WO_4]^{2-}$ groups, such as: high chemical stability, high absorption coefficient and high average refractive index, which signals an efficient transfer of energy from the host matrix of tungstates for the localized states of the doping ions and, therefore, results in greater emission.[37] According to Zhang et al.,[42] the spectral overlap of absorption between donor $[WO_4]^{2-}$, and acceptor ions (Pr^{3+}/Tm^{3+}) is necessary for energy transfer to occur.

Fig. 5(b) shows that the increase of Eu^{3+} concentration favored the luminescent intensity more significantly in the $^5D_0 \rightarrow {}^7F_2$ band. Related to each spectrum, they present digital photos of the emission of $CaWO_4$:Eu^{3+},Tm^{3+}, showing a tendency of emission from orange to red with the increase of Eu^{3+} content. The transition $^5D_0 \rightarrow {}^7F_2$ (624 nm) is predominant from the others, as this behavior indicates that the electric dipole is dominant and that the transition is hypersensitive to the changes that occur around the

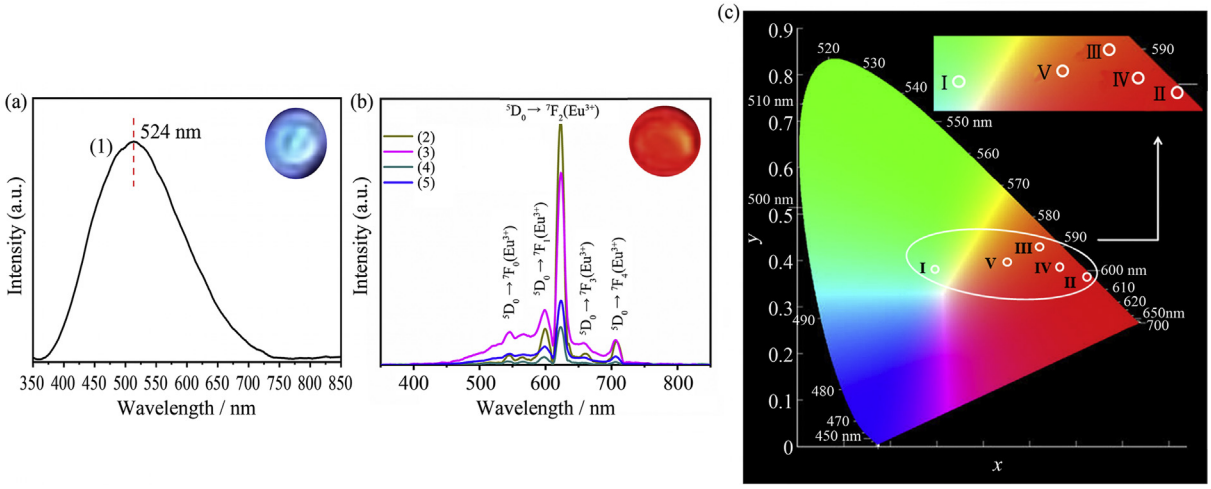

Fig. 5. (a) $CaWO_4$ emission spectrum; (b) $CaWO_4$:4 mol%Eu^{3+} (2), $CaWO_4$:3 mol%Eu^{3+},1 mol%Tm^{3+} (3), $CaWO_4$:2 mol%Eu^{3+},2 mol%Tm^{3+} (4), $CaWO_4$:1 mol%Eu^{3+},3 mol%Tm^{3+} (5) emission spectra; (c) Representation of CIE coordinates in the chromaticity diagram.

Eu^{3+}. This ability of the Eu^{3+} self-assembly makes it known as a spectroscopic probe capable of recording distortions present in the structure.[9] This sensitivity is strongly signaled by the emission intensity of this transition, which corresponds to the symmetry of the host lattice. When Eu^{3+} is located in a low symmetry location, the electric dipole $^5D_0 \rightarrow {}^7F_2$ dominates, while the magnetic dipole transition $^5D_0 \rightarrow {}^7F_1$ corresponds to a reverse centrosymmetry location, according to the Judd-Ofelt theory.[43] The luminance intensity ratio between $^5D_0 \rightarrow {}^7F_2$ (I_2) and $^5D_0 \rightarrow {}^7F_1$ (I_1) is known as symmetry ratio (R): $R = I_2(^7F_2)/I_1(^7F_1)$ reveals the distortion degree of the inversion symmetry of the local environment in the vicinity of Eu^{3+} in the host matrix. The R values were calculated and are recorded in Table 1 in the supplementary material. Intensities I_2 and I_1 are defined as the area below the curve for the respective transitions in order to perform the calculation.

According to the R values found, it is verified that the increase of Eu^{3+} concentration favors the electrical behavior, which indicates a greater asymmetry around the Eu^{3+} ions in $CaWO_4$:Eu^{3+},Tm^{3+}. Ca vacancy (V_{Ca}^{2+}) motivated by the substitution of Ca^{2+} by Eu^{3+}/Tm^{3+} induces a low symmetry due to lattice distortions, which favors the increase of luminescence.

The chromaticity coordinates according to the "Commission Internationale de L'Eclairage" (CIE) were calculated for $CaWO_4$ and $CaWO_4$:Eu^{3+},Tm^{3+} series and are illustrated in the CIE diagram in Fig. 5(c). Other color characterization parameters such as color reproducibility index (CRI), color purity, correlated color temperature (CCT) are listed in Table 1.

The energy level diagrams of the $(WO_4)^{2-}$ group, Tm^{3+} and Eu^{3+} ions and the probable energy transfer process (ET) are shown in Fig. 6. From the excitation of 325 nm UV light, electrons from the $(WO_4)^{2-}$ group absorb energy and move to the conduction band. Part of this energy is transferred to the Tm^{3+} ions at the $^1D_2$ level. The absence of transitions related to Tm^{3+} is verified in the emission spectra, it is reasonable to consider that Tm^{3+} ions transfer directly from their energy to the $^5D_2$ state of Eu^{3+} represented by the ET1 process. Rao et al.[44] observed that the energy between Tm^{3+} ($^1D_2$) and Eu^{3+} ($^1D_2$) in $Sr_2Gd_8(SiO_4)_6O_2$ has been successfully transferred, improving the performance of white light emission. According to Santiago,[45] Tm^{3+} ions are classified as sensitizers because they have higher levels of energy absorption, being able to transfer the absorbed energy to activating ions. In another study Santiago et al.[46] affirmed the transfer of energy due to the spectral overlap of absorption and optical emission between donor ions (Tm^{3+}) and activators (Pr^{3+}). ET2 occurs through the direct

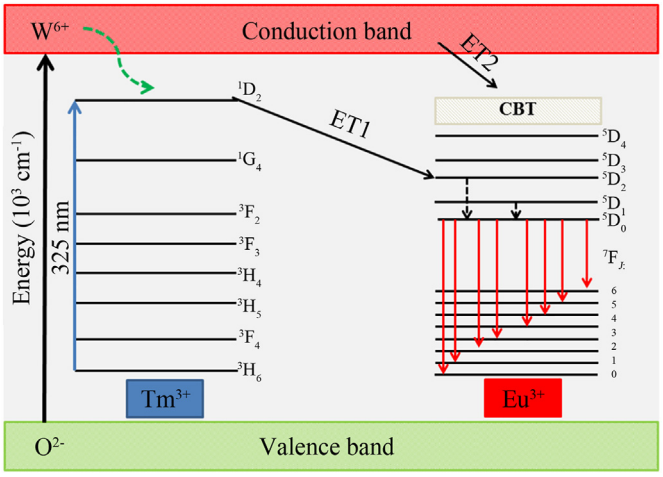

Fig. 6. Energy level diagrams of $(WO_4)^{2-}$ group,Tm^{3+} ion, and Eu^{3+} ion and ET process.

migration of the energy from the $(WO_4)^{2-}$ group to the high-level excited state of the Eu^{3+} ion,[47] which is observed by the photoluminescent properties in Fig. 5 (b).

The purity degree of the color was evaluated, verifying that the increase in the Eu^{3+} concentration promotes a growth in the purity percentage of the red color. Color purity was calculated from Eq. (7),[48]

$$\text{Color purity} = \left(\frac{\sqrt{(x - x_i)^2 + (y - y_i)^2}}{\sqrt{(x_d - x_i)^2 + (y_d - y_i)^2}} \right) \times 100\% \quad (7)$$

where (x, y) are the sample point coordinates, (x_d, y_d) the dominant wavelength coordinates (λ_{dm}) and (x_i, y_i) the white light coordinates in the diagram. The dominant wavelength of each sample is recorded in Table 1. In the present study $(x_d, y_d) = (0.37, 0.63)$ and $(x_i, y_i) = (0.3101, 0.3162)$. $CaWO_4$:Eu^{3+},Tm^{3+} experiences a decrease in color purity with increasing Eu^{3+} concentration. The $CaWO_4$:4 mol%Eu^{3+} sample features a maximum color purity of 97%. The color purity of $CaWO_4$:Eu^{3+},Tm^{3+} is much greater than that of other reported red matches. Given this result, it is reasonable to consider that $CaWO_4$:Eu^{3+},Tm^{3+} has great potential for use as a red-emitting material excited by UV light.

The characteristics presented by the LEDs can vary significantly, bringing several consequences, including the aspect of the quality of color reproduction. CRI is a method of measuring how closely the colors of objects are reproduced when illuminated by a particular light source. According to the estimated CRI for $CaWO_4$ and $CaWO_4$:Eu^{3+},Tm^{3+} series in Table 1, $CaWO_4$:3 mol%Eu^{3+},1 mol% Tm^{3+} performed the best, recording 92% CRI. This result means an excellent color reproduction index very close to the incandescent lamp that is taken as reference, therefore considered with CRI = 100%.

The luminous efficiency of radiation (LER) of the samples was also investigated. The results revealed high LER values (316 lm/W), a characteristic desired for use in WLEDs. The ratio of the emitted luminous flux in lumen and the power used in watts describes LER. LER is a measure expressed in lumens per visible watts used to estimate how brightly the radiation is perceived to be by the average human eye. LER is determined by the spectral distribution $S(\lambda)$ of the source, as given by Eq. (8):

$$\text{LER} = \frac{Km \int_{360}^{830} V(\lambda) S(\lambda) d\lambda}{\int_{360}^{830} S(\lambda) d\lambda} \quad (8)$$

where $V(\lambda)$ = eye sensitivity curve and $Km = 683$ (lm/W), which is the highest possible efficiency that can ever be obtained from a light source.[49] LER decreases as the concentration of Eu^{3+} increases, that is, when the emission band changes to red. This is caused by a smaller overlapping of the emission spectra with the human eye sensitivity curve.[50]

4. Conclusions

$CaWO_4$:Eu^{3+},Tm^{3+} was successfully synthesized by the MAH method. $CaWO_4$:Eu^{3+},Tm^{3+} showing an evolution in the morphologies presented as dopants are introduced. A crystal growth mechanism consisting of the self-assembly and Ostwald-ripening steps for crystal formation were proposed for better understanding. The absorption property occurs in the 200–450 nm band due to the charge transfer process from ligand (O^{2-}) to metal (W^{6+}) (LMCT) in conjunction with Tm^{3+} related electronic excitation

Table 1
Symmetry ratio (R): $R = I_2(^7F_2)/I_1(^7F_1)$, CIE coordinates, CRI[a], color purity, CCT[b], LER[c] and color with varying Eu^{3+} and Tm^{3+} concentrations.

Code	Samples	R	CIE (x, y)	CRI (%)	Color purity (%)	λ_{dm} (nm)	CCT (K)	LER (lm/W)	Color
I	$CaWO_4$	–	(0.29, 0.37)	73	14	505	7226	309	Bluish green
II	$CaWO_4$:4 mol%Eu	5.17	(0.63, 0.35)	92	97	605	1085	259	Red
III	$CaWO_4$:3 mol%Eu,1 mol%Tm	2.36	(0.52, 0.43)	84	92	590	2066	285	Yellowish Orange
IV	$CaWO_4$:2 mol%Eu,2 mol%Tm	3.72	(0.56, 0.37)	76	83	597	1525	279	Reddish Orange
V	$CaWO_4$:1 mol%Eu,3 mol%Tm	0.31	(0.45, 0.38)	68	52	585	2502	316	Orange

[a] Color reprducibility index.
[b] Correlated color temperature.
[c] Luminous eficiency of radiation.

transitions at: $^3H_6 \rightarrow {}^1G_4$ (393 nm), $^3H_6 \rightarrow {}^3F_3$ (687 nm) and $^3H_6 \rightarrow {}^3H_4$ (795 nm), and Eu^{3+} at: $^7F_0 \rightarrow {}^5L_6$ (396 nm), $^7F_0 \rightarrow {}^5D_2$ (467 nm), $^7F_0 \rightarrow {}^5D_1$ (536 nm). The gap energy was estimated to be between 3.20 and 4.14 eV, the observed reduction is associated with the substitution of $Ca^{2+} \rightarrow Eu^{3+}/Tm^{3+}$, inducing defects and distortions that modify the $CaWO_4$ electronic structure. The emission spectra clearly display the $^2D_0 \rightarrow {}^7F_J$ transitions ($J = 0$, 1, 2, 3 and 4) which are characteristic of Eu^{3+}. The maximum intensity of the $^2D_0 \rightarrow {}^7F_2$ transition indicates the electric character domain, that is a hypersensitive transition to distortions around the Eu^{3+} ion. As the Eu^{3+} concentration increases, the displayed color gradually changes from orange to red. $CaWO_4$:4 mol%Eu^{3+} exhibits a very high purity (97%), very close to pure red. Based on the results shown in this paper, $CaWO_4$:Eu^{3+},Tm^{3+} may be a promising red phosphor for white LEDs under UV excitation.

Acknowledgements

The authors thank the following Brazilian research financing institutions for financial support: the National Council for Scientific and Technological Development – (CNPq) Process 303604/2018-2, the Coordination for the Improvement of Higher Education Personnel (CAPES) - Brazil and the Graduate Program in Materials Science and Engineering (PPGCEM/UFRN).

Appendix A. Supplementary data

Supplementary data to this article can be found online at https://doi.org/10.1016/j.jre.2021.01.005.

References

1. Du P, Ran WG, Li WP, Luo LH, Huang XY. Morphology evolution of Eu^{3+}-activated $NaTbF_4$ nanorods: a highly-efficient near-ultraviolet light-triggered red-emitting platform towards application in white light-emitting diodes. *J Mater Chem C*. 2019;7:10802.
2. Mi WX, Zheng J, Qiao P, Cao LL, Chu SQ, Ma HP. Tunable luminescence, energy transfer and excellent thermal stability of $SrMg_2(PO_4)_2$:Ce^{3+},Tb^{3+} phosphors for LEDs. *J Rare Earths*. 2021;39:19.
3. Zhu HT, Liu XH, Fu RL, Shi YH, Wang H, He QJ, et al. Luminous efficiency enhancement of WLEDs via patterned RGB phosphor arrays. *J Lumin*. 2019;211:1.
4. Zhong Y, Gai SJ, Yang YM, Xia M, Zhang Y, Qiu FS, et al. A novel green phosphor $Sr_8ZnY(PO_4)_7$:Eu^{2+},Ln^{3+} (Ln = Pr, Tm, Yb) with broad emission band for high color rendering white-lighting-emitting diodes. *J Lumin*. 2019;214:116600.
5. Fan FY, Zhao L, Shang YF, Liu J, Chen WB, Li YY. Thermally stable double-perovskite Ca_3TeO_6:Eu^{3+} red-emitting phosphors with high color purity. *J Lumin*. 2019;211:14.
6. Guo HF, Shi QF, Ivanovskikh KV, Wang L, Cui CE, Huang P. A high color purity red-emission phosphor based on Sm^{3+} and Eu^{3+} codoped $Ba_3Bi(PO_4)_3$. *Mater Res Bull*. 2020;126:110836.
7. Huang XY, Guo H, Liang J, Wang SY. Synthesis and photoluminescence properties of novel red-emitting $KBaLu(MoO_4)_3$:Eu^{3+} phosphors with high thermal stability and high color purity. *Inorg Chem Commun*. 2020;116:107938.
8. Zheng JH, Feng J, Cheng QJ, Guo ZQ, Cai LH, Chen C. A novel high color purity yellow luminescent material $NaBaBO_3$:Sm^{3+}. *Funct. Mater. Lett.* 2015;8:1550042.
9. Wang CY, Gu CT, Zeng T, Zhang QQ, Luo XP. Bi_2WO_6 doped with rare earth ions: preparation, characterization and photocatalytic activity under simulated solar irradiation. *J Rare Earths*. 2021;39:58.
10. Du CC, Yi GE, Su YG, Liu ZL. Synthesis, characterization, and enhanced luminescence of $CaWO_4$:Eu^{3+}/SBA-15 composites. *J Mater Sci*. 2012;47:6305.
11. Santiago AAG, Tranquilin RL, Botella P, Manjon FJ, Errandonea D, Paskocimas CA, et al. Spray pyrolysis synthesis and characterization of $Mg_{1-x}Sr_xMoO_4$ heterostructure with white light emission. *J Alloys Compd*. 2020;813:152235.
12. Gracia L, Longo VM, Cavalcante LS, Beltrán A, Avansi W, Li MS, et al. Presence of excited electronic state in $CaWO_4$ crystals provoked by a tetrahedral distortion: an experimental and theoretical investigation. *J Appl Phys*. 2011;110, 043501.
13. Lovisa LX, Oliveira MC, Andrés J, Gracia L, Li MS, Longo E, et al. Structure, morphology and photoluminescence emissions of $ZnMoO_4$:RE^{3+} =Tb^{3+} - Tm^{3+} - xEu^{3+} (x = 1, 1.5, 2, 2.5 and 3 mol%) particles obtained by the sonochemical method. *J Alloys Compd*. 2018;750:55.
14. Lee JH. Gas sensors using hierarchical and hollow oxide nanostructures: Overview. *Sens Actuators B*. 2009;140:319.
15. Nie ZH, Petukhova A, Kumacheva E. Properties and emerging applications of self-assembled structures made from inorganic nanoparticles. *Nat Nanotechnol*. 2010;5:15.
16. Larson AC, Von Dreele RB. *General structure analysis system (GSAS)*. Los Alamos: National Laboratory Report LAUR; 2004:86.
17. Taoufyq A, Guinneton F, Valmalette J-C, Arab M, Benlhachemi A, Bakiz B, et al. Structural, vibrational and luminescence properties of the $(1-x)CaWO_4-xCdWO_4$ system. *J Solid State Chem*. 2014;219:127.
18. Cavalcante LS, Longo VM, Sczancoski JC, Almeida MAP, Batista AA, Varela JA, et al. Electronic structure, growth mechanism and photoluminescence of $CaWO_4$ crystals. *CrystEngComm*. 2012;14:853.
19. Basiev TT, Sobol AA, Voronko YuK, Zverev PG. Spontaneous Raman spectroscopy of tungstate and molybdate crystals for Raman lasers. *Opt Mater*. 2000;15:205.
20. Campos AB, Simões AZ, Longo E, Varela JA, Longo VM, de Figueiredo AT, et al. Mechanisms behind blue, green, and red photoluminescence emissions in $CaWO_4$ and $CaWO_4$ powders. *Appl Phys Lett*. 2007;91, 051923.
21. Longo VM, Cavalcante LS, Erlo R, Mastelaro VR, de Figueiredo AT, Sambrano JR, et al. Strong violet–blue light photoluminescence emission at room temperature in $SrZrO_3$: joint experimental and theoretical study. *Acta Mater*. 2008;56:2191.
22. Almeida MAP, Lima JRO, Morila-Santos C, Lisboa Filho PN, Siu Li M, Longo E, et al. Effect of Zn^{2+} ions on the structure, morphology and optical properties of $CaWO_4$ microcrystals. *J Sol Gel Sci Technol*. 2014;72:648.
23. Chen YQ, Moon BK, Choi BC, Jeong JH, Yang HK. Growth mechanism and photoluminescence investigation of double-broccoli-like $CaWO_4$:Eu^{3+} superstructures via hydrothermal synthesis. *J Am Ceram Soc*. 2013;96:3596.
24. Tian Y, Chen BJ, Yu HQ, Hua RN, Li XP, Sun JS, et al. Controllable synthesis and luminescent properties of three-dimensional nanostructured $CaWO_4$:Tb^{3+} microspheres. *J Colloid Interface Sci*. 2011;360:586.
25. Liu SH, Tian SF, Xing RM. $CaWO_4$ hierarchical nanostructures: hydrothermal synthesis, growth mechanism and photoluminescence properties. *CrystEngComm*. 2011;13:7258.
26. Cavalcante LS, Sczancoski JC, Tranquilin RL, Varela JA, Longo E, Orlandi MO. Growth mechanism of octahedron-like $BaMoO_4$ microcrystals processed in microwave-hydrothermal: experimental observations and computational modeling. *Particuology*. 2009;7:353.
27. Zhang HZ, Gilbert B, Huang F, Banfield JF. Water-driven structure transformation in nanoparticles at room temperature. *Nature*. 2003;424:1025.
28. Gonçalves RF, Cavalcante LS, Nogueira IC, Longo E, Godinho MJ, Sczancoski JC, et al. Rietveld refinement, cluster modelling, growth mechanism and photoluminescence properties of $CaWO_4$:Eu^{3+} microcrystals. *CrystEngComm*. 2015;17:1654.
29. da Silva LF, Catto AC, Avansi Jr W, Cavalcante LS, Andrés J, Aguir K, et al. A novel ozone gas sensor based on one-dimensional (1D) α-Ag_2WO_4 nanostructures. *Nanoscale*. 2014;6:4058.
30. Abraham Y, Holzwarth NAW, Williams RT. Electronic structure and optical properties of $CdMoO_4$ and $CdWO_4$. *Phys Rev B*. 2000;62:1733.
31. Suzuki K, Kijima K. Optical band gap of barium titanate nanoparticles prepared by RF-plasma chemical vapor deposition. *J Appl Phys*. 2005;44:2081.

32. Zhang Y, Holzwarth NAW, Williams RT. Electronic band structures of the scheelite materials $CaMoO_4$, $CaWO_4$, $PbMoO_4$, and $PbWO_4$. *Phys Rev B Condens Matter*. 1998;57:12738.
33. Xia ZG, Zhuang JQ, Liu HK, Liao LB. Photoluminescence properties and energy transfer of $Ba_2Lu(BO_3)_2Cl:Eu^{2+}/Eu^{3+},Tb^{3+}$ phosphors. *J Phys D: Appl Phys*. 2012;45:015302.
34. Orhana E, Anicete-Santos M, Mama Maurera, Pontes FM, Souza AG, Andrés J, et al. Towards an insight on the photoluminescence of disordered $CaWO_4$ from a joint experimental and theoretical analysis. *J Solid State Chem*. 2005;178:1284.
35. Patil PN, Subramanian U, Jeyakanthan M. Enhanced blue emission of $CaWO_4$ in $BaWO_4/CaWO_4$ nanocomposite. *J Mater Sci: Mater Electron*. 2020;31:7260.
36. Mikhailika VB, Kraus H, Miller G, Mykhaylyk MS, Wahl D. Luminescence of $CaWO_4$, $CaMoO_4$, and $ZnWO_4$ scintillating crystals under different excitations. *J Appl Phys*. 2005;97, 083523.
37. Maheshwary, Singh BP, Singh J, Singh RA. Luminescence properties of Eu^{3+}-activated $SrWO_4$ nanophosphors-concentration and annealing effect. *RSC Adv*. 2014;4:32605.
38. Chen YQ, Yang HK, Park SW, Moon BK, Choi BC, Jeong JH, et al. Characterization and photoluminescent enhancement of Li^+ corporation effect on $CaWO_4:Eu^{3+}$ phosphor. *J Alloys Compd*. 2012;511:123.
39. Lokeswara Reddy GV, Rama Moorthy L, Packiyaraj P, Jamalaiah BC. Optical characterization of $YAl_3(BO_3)_4:Dy^{3+}$–Tm^{3+} phosphors under near UV excitation. *Opt Mater*. 2013;35:2138.
40. Du P, Guo Y, Lee S-H, Yu J-S. Broad near-ultraviolet and blue excitation band induced dazzling red emissions in Eu^{3+}-activated Gd_2MoO_6 phosphors for white light-emitting diodes. *RSC Adv*. 2017;7:3170.
41. Shi SK, Gao J, Zhou J. Effects of charge compensation on the luminescence behavior of Eu^{3+} activated $CaWO_4$ phosphor. *Opt Mater*. 2008;30:1616.
42. Zhang XS, Yao CZ, Li LF, Yan CY, Wei BH. Facile fabrication and spectroscopic study of the energy transfer effect of Pr^{3+} and Tm^{3+} codoped La_2O_3 nanorod arrays. *Matter Lett*. 2012;76:165.
43. Shionoya S, Yen WM, Yamamoto H. *Phosphor handbook*. Boca Raton: CRC Press; 2007.
44. Rao GM, Raju GSR, Hussain SK, Pavitra E, Psv Subba Rao J-S Yu. Tunable emissions via the white region from $Sr_2Gd_8(SiO_4)_6O_2:RE^{3+}$ (RE^{3+}: Dy^{3+}, Tm^{3+}, Eu^{3+}) phosphors. *New J Chem*. 2016;40:6214.
45. Santiago AAG, Lovisa LX, Medeiros PN, Li MS, Carreño NLV, Longo E, et al. Fast and simultaneous doping of $Sr_{0.9-x-y-z}Ca_{0.1}In_2O_4:(xEu^{3+}, yTm^{3+}, zTb^{3+})$ superstructure by ultrasonic spray pyrolysis. *Ultrason Sonochem*. 2019;56:14.
46. Santiago AAG, Macedo EM, Oliveira FKF, Motta FV, Bomio MRD. Synthesis and characterization of $BaWO_4:xTm^{3+},yPr^{3+}$ obtained by ultrasonic spray pyrolysis. *J Mater Sci: Mater Electron*. 2020;31:11599.
47. Cao RP, Xu HD, Peng DD, Jiang SH, Luo ZY, Li WS, et al. Synthesis, luminescence properties, and energy transfer of novel $CaWO_4:Eu^{3+},Mn^{2+}$ red phosphor. *Superlattice Microst*. 2015;88:5.
48. Wu Y-F, Nien Y-T, Wang Y-J, Chen I-G. Enhancement of photoluminescence and color purity of $CaTiO_3$:Eu phosphor by Li doping. *J Am Ceram Soc*. 2012;95:1360.
49. Katelnikovas A, Winkler H, Kareiva A, Jüstel T. Synthesis and optical properties of green to orange tunable garnet phosphors for pcLEDs. *Opt Mater*. 2011;33:992.
50. Liu XG, Li L, Noh H-M, Moon B-K, Choi B-C, Jeong J-H. Chemical bond properties and charge transfer bands of O^{2-}–Eu^{3+}, O^{2-}–Mo^{6+} and O^{2-}–W^{6+} in Eu^{3+}-doped garnet hosts $Ln_3M_5O_{12}$ and ABO_4 molybdate and tungstate phosphors. *Dalton Trans*. 2014;43:8814.